Check for updates

ADVANCED THERAPEUTICS
www.advtherap.com

Magnetic Mesoporous Janus Microrollers for Combined Chemo- and Photothermal Ablation Therapy

*Gulsen Aybar Tural, Ugur Bozuyuk, Nihal Olcay Dogan, Yunus Alapan, Mukrime Birgul Akolpoglu, Amirreza Aghakhani, Jelena Lazovic, Ozgen Ozer, and Metin Sitti**

Mobile microrobots have been proposed as a promising approach to overcome the limitations of traditional drug/gene delivery systems. Magnetically actuated surface rolling microrobots, or magnetic surface microrollers, have shown potential for navigation in physiologically relevant environments due to their robust locomotion characteristics. Although much is known about their locomotion abilities in various environments, the full extent of their potential in medical applications has yet to be fully explored. Here, the potential of surface microrollers for combined chemo- and photothermal ablation therapy under medical imaging modalities is demonstrated. The surface microrollers are half-coated with magnetic material, allowing for photothermal heating and magnetic locomotion, and loaded with a biopharmaceutics classification system (BCS) class IV anti-cancer drug, Docetaxel (DTX), for combined therapy. Synergistic action of on-demand photothermal ablation and the controlled release of DTX result in the efficient elimination of cancer cells. Furthermore, microrollers can be detected ex vivo with magnetic resonance imaging (MRI) and photoacoustic imaging (PA), highlighting the potential of surface microrollers for future targeted medical applications.

1. Introduction

Non-specific distribution in the body is one of the major drawbacks of the drug/gene delivery systems currently in use, which results in off-site side effects and fundamentally limits the administration dose.[1] Mobile microrobots have been proposed to overcome these limitations due to their active targeting ability and precise controllability.[2–4] Thus far, a significant research effort has been made for the development of medical microrobots to explore novel actuation mechanisms,[5] drug delivery,[6] biocompatibility,[7,8] and medical imaging.[9]

Magnetically actuated surface rolling microrobots, also known as magnetic surface microrollers, are a robust microrobotic platform that has shown great promise for navigation in physiologically relevant environments due to their strong propulsion capability.[10–16] While the locomotion capability of microrollers has been extensively studied for in vivo navigation in different biophysical environments, further research is needed to expand their medical functionality beyond locomotion for specific medical applications. To address this issue, integrating multimodal synergistic therapies appears to be a promising approach for microrollers. Multimodal synergistic therapies have gained considerable attention in the past decade thanks to their superior treatment capabilities over monotherapies.[17] This approach involves integrating different mechanisms into a single platform, resulting in much higher therapeutic efficiency than individual treatments.[17] Chemotherapy is a conventional method for treating cancer, while thermal therapies have recently been introduced as adjuvant therapies.[18] Combining these modalities can be beneficial in terms of increasing each other's efficiency or reducing the required dose of chemotherapeutic agents or thermal energy.[19]

Here, we demonstrate combined chemotherapy and photothermal ablation applications using microrollers. The magnetic microrollers were composed of mesoporous 3 μm silica particles, half coated with a magnetic nickel (Ni) layer, enabling not only magnetically powered locomotion but also photothermal heating of the microrollers along with the gold (Au) layer. The mesopores of the microrollers were loaded with a model BCS class IV (low solubility, low permeability) anti-cancer drug, DTX,[20] for

G. Aybar Tural, U. Bozuyuk, N. O. Dogan, Y. Alapan, M. B. Akolpoglu, A. Aghakhani, J. Lazovic, M. Sitti
Physical Intelligence Department
Max Planck Institute for Intelligent Systems
70569 Stuttgart, Germany
E-mail: sitti@is.mpg.de

G. Aybar Tural, O. Ozer
Faculty of Pharmacy
Department of Pharmaceutical Technology
Ege University
Izmir 35040, Turkey

U. Bozuyuk, N. O. Dogan, M. B. Akolpoglu, M. Sitti
Institute for Biomedical Engineering, ETH Zurich
Zurich 8092, Switzerland

M. Sitti
School of Medicine and College of Engineering
Koç University
Istanbul 34450, Turkey

The ORCID identification number(s) for the author(s) of this article can be found under https://doi.org/10.1002/adtp.202300319

© 2023 The Authors. Advanced Therapeutics published by Wiley-VCH GmbH. This is an open access article under the terms of the Creative Commons Attribution License, which permits use, distribution and reproduction in any medium, provided the original work is properly cited.

DOI: 10.1002/adtp.202300319

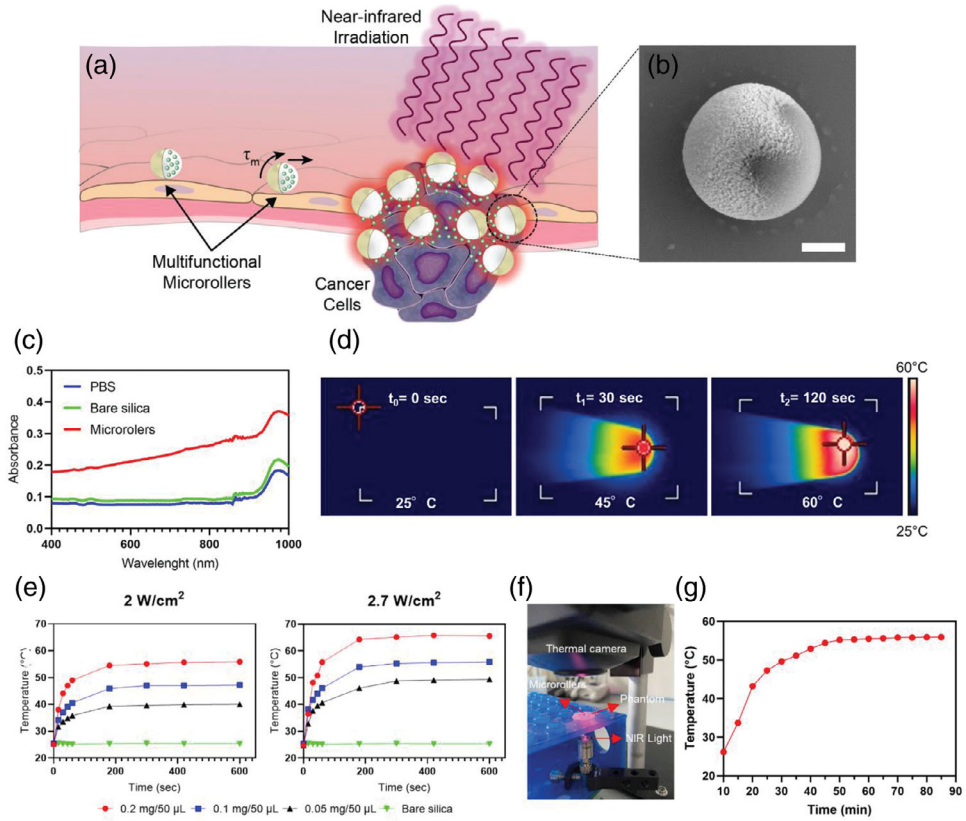


Figure 1. Magnetic microrollers for combined chemotherapy and photothermal ablation. A) Conceptual schematic depicts the magnetic actuation of the microrollers and the thermal ablation during the drug release at the target tumor site. B) SEM image of the microroller; scale bar: 1 µm. C) Light absorption spectra of the microrollers and bare silica particles. The light absorption of microrollers was at least two times higher than the bare silica particles and PBS at all wavelengths. D) Thermal camera images of the heated microrollers (0.2 mg/50 µL, 2.7 W cm^{-2} NIR light intensity) at different time points. In the beginning, both the tube and the room were at 25 °C. Therefore, the image appeared blank. Upon NIR irradiation, Janus microrollers started to heat. E) Photothermal heating profile of the microrollers at 2 and 2.7 W cm^{-2} NIR light intensity at 808 nm. F) Photothermal heating setup with the phantom. G) Photothermal heating profile of microrollers with the phantom.

tandem chemotherapeutic action along with photothermal ablation at the tumor site (**Figure** 1A). We demonstrated that the combined DTX delivery and photothermal ablation effectively induced cell death in T-47D breast cancer cells more efficiently than monotherapies individually. We also showed that the microroller amount required for effective combined therapy was detectable ex vivo using magnetic MRI and PA, further highlighting their in vivo potential. Overall, our study highlights the potential of microrollers as a versatile platform for targeted medical interventions. The integration of chemotherapy and photothermal ablation within a single targeted carrier system, as demonstrated here, offers new opportunities for improving treatment outcomes, reducing side effects, and advancing the field of cancer therapeutics.

2. Results and Discussions

2.1. Heating Profile of Janus Microrollers

We selected mesoporous silica particles with 3 µm particle size and 4 nm pore size as a microroller body, which were half coated sequentially with Ni and Au layers. While the Ni layer provides the magnetic response under dynamically changing uniform magnetic fields, the Au layer prevents the Ni layer from oxidation, and provides biocompatibility.[10] Janus particle formation was confirmed with scanning electron microscopy (SEM) analysis (Figure 1B). To provide additional visual information and confirm the presence of mesopores within the silica side, we employed transmission electron microscopy (TEM) imaging in scanning (STEM) mode (Figure S1A, Supporting Information).

Half-coated metallic layers on microrollers also allow efficient absorption of external light and conversion into thermal energy by activating the electrons, resulting in the heating of the microrollers and the surrounding medium.[21] We performed spectrophotometric analysis to characterize the absorbance of the microrollers in comparison with bare silica particles and phosphate buffered saline (PBS, 1×). The absorbance values recorded from 400 to 1000 nm wavelengths showed greater absorbance of microrollers than bare silica particles and PBS at all wavelengths, with increasing differences closer to the infrared region (Figure 1C).

We further assessed the photothermal capacity of the microrollers at different concentrations by monitoring the temperature change from room temperature with a thermal infrared

© 2023 The Authors. Advanced Therapeutics published by Wiley-VCH GmbH

23663987, 2024, 2, Downloaded from https://onlinelibrary.wiley.com/doi/10.1002/adtp.202300319 by Koc University, Wiley Online Library on [26/02/2024]. See the Terms and Conditions (https://onlinelibrary.wiley.com/terms-and-conditions) on Wiley Online Library for rules of use; OA articles are governed by the applicable Creative Commons License

camera under constant near infrared (NIR) light irradiation (808 nm, Figure 1D). Precise irradiation of the microrollers was ensured by immobilizing them at the bottom of microcentrifuge tubes via a permanent magnet (Figure S2, Supporting Information). The power density of NIR light was fixed to 2 and 2.7 W cm^{-2}, which are in the range for the safe use of NIR light in photothermal therapies.[22] At the power density of 2 W cm^{-2}, only the concentration of 0.2 mg/50 µL could exceed 50 °C, which is the minimum required temperature for thermal ablation (Figure 1E).[23] At the power density of 2.7 W cm^{-2} the concentrations of 0.2 mg/50 µL and 0.1 mg/50 µL exceeded the 50 °C. The concentration of 0.2 mg/50 µL reached 65.2 °C within 5 min and remained stable until the end of the heating (Figure 1E). According to the literature, biological effects such as protein denaturation, membrane rupture, and cell shrinkage occur between 60–140 °C.[22] Enzyme inactivation and mitochondrial injury occur between 42–60 °C.[24] Thus, we decided to continue further tests with the concentration of 0.2 mg/50 µL at 2.7 W cm^{-2} power density to reach the highest temperature.

To further evaluate the photothermal capacity of microrollers for in vivo applications, we prepared a physiologically relevant phantom mimicking the light scattering and absorption characteristics of the dermis layer of the skin as described in the literature.[25] We fixed the phantom above the NIR light source at 2 cm distance, and microrollers (0.2 mg/50 µL) were positioned at the center of the phantom (Figure 1F). The same power density (2.7 W cm^{-2}) was applied while monitoring the temperature change with the thermal infrared camera (Figure 1G). Microrollers were heated up to as high as 55.8 °C from room temperature within 55 min and remained stable until the end of the heating. Despite the reduction in photothermal efficiency, the temperature elevation of approximately 30.8 °C would still permit effective heating in physiologically relevant conditions for photothermal ablation. Elevated temperatures or shorter heating times could be achieved by using different collimators or light sources with greater power density output.

2.2. DTX Loading and Release Studies

DTX was loaded into the mesopores of the silica side of the microrollers by the well-established solvent evaporation technique (**Figure 2A**). This technique relies on the diffusion of drug molecules from the solvent to mesopores.[26] Briefly, silica is dispersed in a volatile organic solution containing the drug and then dried quickly under vacuum, allowing sufficient time for the drug to diffuse into the pores.[27] Once the loading procedure is completed, the drug loaded silica particles are washed three times to remove any remaining unloaded drug. Due to the competitive adsorption of polar solvents on the silica surface, resulting in limited drug adsorption, nonpolar solvents are more favorable for efficient loading of DTX.[28,29] Yet safety issues, according to the International Council for Harmonisation (ICH) guidelines, ease of removal of the solvents, and the solubility of the drug also should be considered. We chose three solvents from the ICH Guideline for Residual Solvents (Q3C(R8)),[30] in which Class 1 refers to "solvents to be avoided," Class 2 refers to "solvents to be limited," and Class 3 refers to "solvents with low toxic potential." We selected ethanol (Class 3), dichloromethane (DCM, Class 2), and hexane (Class 2) with high, moderate, and low polarity, respectively (**Table 1**).[31] While low polarity of hexane is attractive for loading, insolubility of DTX necessitates a mixture of hexane with other solvents with greater polarity. We prepared mixtures of DCM and hexane at 2:1 and 1:1 (v/v) ratios. DTX was fully dissolved in the 2:1 solution, but white precipitates were observed in the 1:1 mixing ratios. Thus, a 2:1 DCM:hexane mixture was used in further drug loading studies.

DTX loading via solvent evaporation in different solvents was first investigated using fluoresecent microscopy. Nile red was used as a model lipophilic cargo. Nile red is a solvatochromic molecule, meaning its fluorescence and the solution's color depend on the medium's polarity (Figure S3A, Supporting Information).[32,33] Fluorescence microscopy images showed that Nile red was only loaded with a DCM and DCM:hexane mixture, while it could not diffuse into the mesopores of silica particles when distributed in ethanol (Figure 2B). The fluorescent images were also consistent with those in Figure S3B, Supporting Information, which showed that silica particles loaded with DCM and DCM:hexane appeared purple, whereas those loaded with ethanol had a pale color indicating that loading was unsuccessful. As a quantitative comparison, a validated high-performance liquid chromatography (HPLC) method was used to compare the encapsulation efficiencies (EE%, Equation (1)) between DCM and DCM:hexane. EE% was calculated at 12% and 17% for DCM and DCM:hexane, respectively. Further studies were performed with 2:1 DCM:hexane due to the observation of higher EE% when DCM and hexane mixtures were used as a solvent.

Drug loading capacity and efficiency were further estimated and confirmed via thermal gravimetric analysis (TGA),[34,35] which measures the weight loss of samples as the temperature is gradually increased.[27] Both bare silica and DTX-loaded silica particles showed weight loss at regions below 100 °C, which is typical for water evaporation (Figure 2C). From 100 to 350 °C, bare silica lost only 0.9% of its weight, whereas DTX-loaded silica lost 11.3%, proving the presence of DTX in the mesoporous silica particles. Multi-point Brunauer–Emmett–Teller (BET) method was used for analyzing the pore volume, pore size of bare silica particles, and the specific surface area of both DTX-loaded and bare silica particles. The pore volume and the pore size of bare silica particles were 0.425 cm^3 g^{-1} and 44 256 Å (4.425 nm), respectively. The surface areas of the bare silica particles and DTX loaded particles were 362.198 and 59.047 m^2 g^{-1}, respectively. As shown in 7-point BET linear plots in Figure 2D, the absorbed volume (cm^3 g^{-1}) of DTX-loaded silica was smaller than the bare silica at all pressure values, confirming the successful DTX loading into the mesopores of silica microparticles. When the unloaded and DTX-loaded surface areas of silica particles were compared, a significant reduction in available pores was evident. Nonetheless, 16% of the pore area remained accessible for N_2 adsorption. This substantial decrease in the BET surface area further indicates that a considerable amount of DTX has penetrated and filled the mesopores.[36] Attenuated total reflectance Fourier transform infrared spectroscopy (ATR FT-IR) analysis was conducted to analyze molecular interactions between DTX and bare silica before and after DTX loading. The spectra were recorded from 3500 to 400 cm^{-1} (Figure 2E). The stretching vibrations of Si—O—Si at 1059 and 806 cm^{-1} and the bending vibrations of Si—O—Si at 451 cm^{-1} were characteristic

© 2023 The Authors. Advanced Therapeutics published by Wiley-VCH GmbH

23663987, 2024, 2, Downloaded from https://onlinelibrary.wiley.com/doi/10.1002/adtp.202300319 by Koc University, Wiley Online Library on [26/02/2024]. See the Terms and Conditions (https://onlinelibrary.wiley.com/terms-and-conditions) on Wiley Online Library for rules of use; OA articles are governed by the applicable Creative Commons License

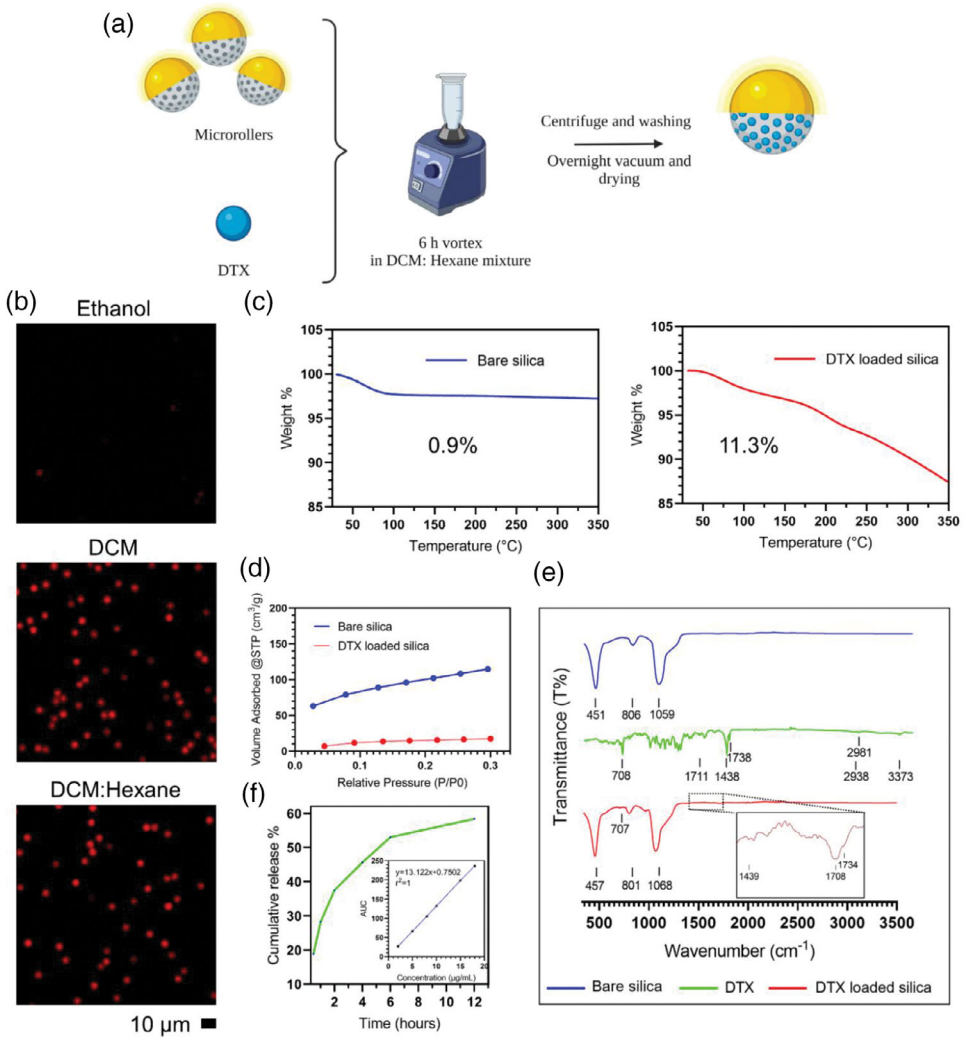


Figure 2. Drug loading and release studies. A) Conceptual schematic of solvent evaporation technique to load DTX into the mesopores of the Janus microrollers. B) Fluorescence microscopy images of lipophilic fluorescence dye, Nile red, loaded bare silica particles via different solvents. Nile red was loaded only with DCM and DCM:hexane mixture. C) TGA of bare silica and DTX loaded silica. Bare silica lost only 0.9% of its weight whereas DTX loaded silica lost 11.3%. D) BET analysis of bare silica and DTX loaded silica. Absorbed volume ($cm^3\ g^{-1}$) of DTX loaded silica was smaller than the bare silica at all pressure values. E) ATR FT-IR spectra of bare silica, DTX, and DTX loaded silica. DTX loaded silica showed the characteristic bands of both silica and DTX. F) Cumulative drug release of DTX loaded microrollers. DTX release matches the Krosmeyer–Peppas model. The error bars represent the standard deviation of the mean. However, error bars are not visible due to the very low standard deviation as presented in Note S1 and Table S1, Supporting Information.

Table 1. Key characteristics of the solvents.[31]

Solvent	Relative polarity	ICH Q3C(R8) class	Evaporation temperature [°C]	DTX solubility
Ethanol	0.654	3	78.37	+
DCM	0.309	2	39.6	+
Hexane	0.009	2	69	–

absorption bands of silica (Figure 2E).[27,37] DTX showed bands at 3373 cm^{-1} (νO-H and νN-H), 1438 cm^{-1} (νC = C), 2981 cm^{-1} (ν_{as}CH), 2938 cm^{-1} (ν_{s}CH), 708 cm^{-1} (δCH), two bands assigned to the vibrational mode νC = 0, one at 1738 cm^{-1} and another at 1711 cm^{-1} relative to the carbonyl groups of ester and ketone, respectively (Figure 2E).[38,39] DTX loaded silica showed the characteristic bands of both silica and DTX at 457, 801, 1068, and 707, 1439, 1708, 1734 cm^{-1}, respectively. The band at 3373 cm^{-1} disappeared due to hydrogen bonding formed by the interaction of the N-H of DTX and -OH of silica, further confirming the interaction of DTX with silica material. The literature has highlighted the significance of understanding the physical state of a drug within a mesoporous system. This is particularly important because, in cases where a poorly soluble drug is located on the external surface, it has the potential to impede the release of the loaded drug.[40] When a drug is loaded into a mesoporous structure, it may exist in an amorphous or nanocrystal form due to its confinement in a few nm wide area.[27] The physical

© 2023 The Authors. Advanced Therapeutics published by Wiley-VCH GmbH

23663987, 2024, 2, Downloaded from https://onlinelibrary.wiley.com/doi/10.1002/adtp.202300319 by Koc University, Wiley Online Library on [26/02/2024]. See the Terms and Conditions (https://onlinelibrary.wiley.com/terms-and-conditions) on Wiley Online Library for rules of use; OA articles are governed by the applicable Creative Commons License

constraints imposed by the pore walls inhibit the growth of drug crystals inside the pores.[40] However, such constraints do not apply outside the pores, allowing larger crystal growth to occur.[40] To differentiate between the drug located outside the pores and the drug inside the pores, analysis of crystals is required, which is accomplished using X-ray powder diffraction (XRD) and differential scanning calorimetry (DSC).[35,40,41] DSC is advantageous due to being highly sensitive in small crystal size.[40] According to the literature, it is possible to differentiate the drug located inside the pores by its lack of contribution to the normal melting endotherm. When the drug crystallizes inside the pores, it leads to a depressed melting endotherm owing to the small crystal size.[35] Conversely, if the drug is in an amorphous form, this may result in absence of melting or glass transition peaks in the DSC thermogram.[35] Likewise, the powder XRD pattern will not show characteristic peaks of crystal structure since the loaded drug cannot crystallize within the mesoporous structure, given that the size of the critical nucleus exceeds the pore size.[27,29,40] DSC and XRD were used to characterize the physical state of the loaded DTX. As shown in Figure S4, Supporting Information, DTX alone showed two endotherms in accordance with the literature.[42] When the DTX loaded into silica mesopores, endotherm peaks disappeared in the DSC thermogram (Figure S4, Supporting Information), and the characteristic peaks of crystal structure mostly became invisible in the XRD pattern as expected (Figure S5). Consequently, while FT-IR, TGA, BET, and HPLC EE% analyses proved the DTX presence within the silica particles, DSC and XRD analyses showed the loaded DTX was in amorphous or tiny crystal form, which was desired to obtain high dissolution rates with poorly soluble drugs.

Next, we characterized drug release profile of DTX from the microrollers. As shown in Figure 2F, DTX showed an initial burst release of 28.2% during the first hour and released 58.4% of the amount loaded within 12 h. This phenomenon can be attributed to the amorphous or nanocrystal state of the drug within the mesopores, which reduces lattice energy and enhances wettability, consequently leading to increased dissolution rates.[40,43] The significant advantage of mesoporous systems lies in their large surface area, which allows for drug dispersion at the molecular level.[43] It has been reported that a monolayer can form on the pores of the particles located on the surface due to interactions between the silanol groups and the drug,[43] including hydrogen bonds, as indicated in the ATR FT-IR analysis (Figure 2E). Therefore, the burst release of DTX can be attributed to the adsorbed DTX on the pores at outermost surface of silica particles, consistent with existing literature.[44–46] The DTX release matches the Krosmeyer–Peppas model. Figure S6, Supporting Information shows the fitting profile of DTX release microrollers with the Krosmeyer–Peppas model. The main mechanisms for drug release are diffusion, erosion, swelling of the polymer matrix, and degradation of the polymer.[47] Because silica is neither degradable nor able to change its morphology by swelling or erosion, the release of the DTX from silica particles depends on diffusion, as proven by the n value being smaller than 0.5 (Figure S6, Supporting Information).[40,48,49] Thanks to their mesoporous structure and large surface area (362.198 m^2 g^{-1}), high dissolution rates are expected, especially for BCS Class II and IV drugs, such as DTX.[40] In our study, we aimed for a high dissolution rate to achieve the maximum possible synergistic effect during photothermal ablation. Besides, the release of the drug from a porous structure depends on the pore size and network, among other physical properties. By changing the porosity and size of the silica particles, tailor-made drug release according to specific purposes could be achieved.[50]

2.3. Magnetic Locomotion Characterization

Microrollers are made out of mesoporous silica particles (average diameter of 3 μm) half coated with 540 nm Ni and 50 nm Au (**Figure 3A**), pre-magnetized in an out-of-plane direction (toward the metallic cap).[10,13] We characterized the magnetic properties of the microrollers using a vibrating sample magnetometer (VSM), in an out-of-plane direction to the surface plane. The analyses revealed that the coercivity (H_c) of the deposited magnetic material is around 13.5 mT for 540 nm Ni (Figure 3B). This meant that the magnetic material on the microrollers would retain its magnetization under field magnitudes of 13.5 mT. Therefore, we actuated the microrollers using 10 mT uniform rotating magnetic fields to preserve encoded magnetization directions. Microrollers followed the external rotating magnetic fields, and the rotation of the microroller bodies resulted in a translational motion by the presence of a nearby wall in low Reynolds number regime.[51] The translational velocity of the microrollers linearly increased with the rotation frequency applied, and they did not step-out until 100 Hz, which was the highest actuation frequency used in the study (Figure 3C). Additionally, we showed that the microrollers could be precisely steered by changing the orientation of the rotating magnetic field, providing complete spatial control (Figure 3D, Movie S1, Supporting Information). When 0.2 mg or 7.8×10^6 microrollers were added onto cancer cell monolayers grown in vitro, the microroller swarms also demonstrated robust propulsion ability at 100 Hz (Figure 3E, Movie S2, Supporting Information).

2.4. In Vitro Cell Culture Studies

2.4.1. Biocompatibility Test

Biocompatibility of DTX free microrollers was evaluated to ensure that the cytotoxic effect is solely due to the DTX and photothermal ablation. Therefore in vitro cytotoxicity tests which are described in the ISO 10993–5 Biological Evaluation of Medical Devices, Part 5: Tests for in vitro cytotoxicity and the United States Pharmacopeia (USP) Biological Reactivity Tests, In vitro Monograph,[52,53] were conducted. We performed extract test as recommended in the USP for high density materials. NIH/3T3 cells were used as a healthy cell line, and T-47D cells were used as a model breast cancer cell line. The extract test was performed under exaggerated conditions, where DTX free microrollers were dispersed in sterile PBS 1× and after the agitation (24 and 48 h), supernatants collected from the microroller solutions were diluted with cell culture medium to obtain different concentrations (0.05–0.2 mg/50 μL). After 24 h of incubation with the extract solution of the microrollers, viability of cells was analyzed based on their adenosine triphosphate (ATP) levels as described previously.[54] Cell viability in all concentrations was higher than

© 2023 The Authors. Advanced Therapeutics published by Wiley-VCH GmbH

23663987, 2024, 2, Downloaded from https://onlinelibrary.wiley.com/doi/10.1002/adtp.202300319 by Koc University, Wiley Online Library on [26/02/2024]. See the Terms and Conditions (https://onlinelibrary.wiley.com/terms-and-conditions) on Wiley Online Library for rules of use; OA articles are governed by the applicable Creative Commons License

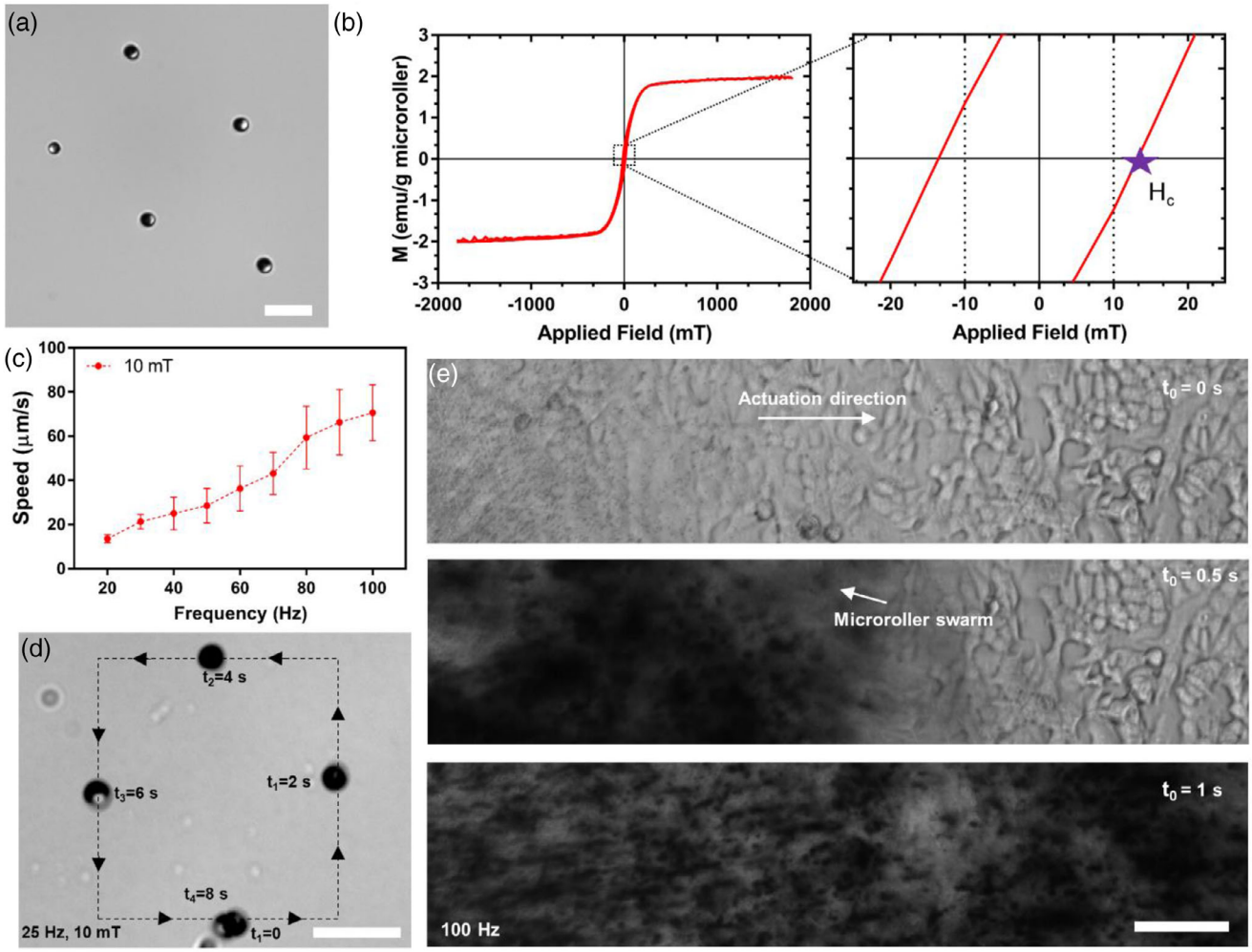


Figure 3. Magnetic and locomotion characterization of microrollers. A) Light microscopy image of a group of microrollers. The microrollers are composed of porous silica microparticles with an average diameter of 3 μm, half coated with 540 nm Ni and 50 nm Au. Scale bar: 10 μm. B) Vibrating sample magnetometer (VSM) characterization of 1.5 mg microrollers. The VSM analysis was performed in an out-of-plane direction and the coercivity of the deposited magnetic material is around 13.5 mT. C) Average translational speeds of the microrollers against increasing rotation frequencies at a 10 mT rotating magnetic field. The microrollers did not step out until 100 Hz. The error bars represent the standard deviation of the mean. D) A single microroller translating under rotating magnetic fields. Trajectory of the microroller was controlled by changing the direction of the field rotation axis (25 Hz, 10 mT). Scale bar: 10 μm. E) Time lapse images of swarming microrollers locomoting over the cancer cells used in the study. At $t_0 = 0$, microroller swarms are not in the field of view. Upon actuation with 100 Hz, they fully covered the cells. Scale bar: 50 μm.

70%, which is the cytotoxicity limit according to ISO 10993–5 (**Figure** 4A).[53] The results indicate no toxic matter was released from the DTX free microrollers during the treatment even though the treatment period (24–48 h) was more extended than the intended application duration (40 min). The biocompatibility tests were conducted following the guidelines published by authorized institutions.[52,53,55] These guidelines recommend the use of rodent fibroblast cells, which are known to be among the sensitive cell types and meet the requirement of a population doubling time less than 30 h.[55,56] Although Janus microrollers demonstrated biocompatibility under in vitro conditions, this finding underscores their potential. However, for comprehensive assessments, including acute and chronic toxicity as well as excretion, in vivo studies are required and planned for future studies.

2.4.2. Photothermal Ablation

Photothermal ablation studies were performed with four different groups: i) NIR applied group without any microrollers, to evaluate the NIR effect alone; ii) DTX loaded microrollers (0.2 mg/50 μL) without NIR to investigate the DTX effect alone; iii) NIR applied group with DTX free microrollers (0.2 mg/50 μL) to evaluate the effect of photothermal ablation alone; and iv) NIR applied group with DTX loaded microrollers (0.2 mg/50 μL) to evaluate the synergistic effect of DTX and photothermal ablation (Figure 4B). After the cells were centrifuged with or without the microrolles, NIR light (2.7 W cm^{-2}) was applied for 40 min to the groups (i), (iii), and (iv), while group (ii) was kept in the incubator. At the end of 40 min, cells were separated from microrollers via a permanent magnet and seeded back for 24 and 48 h of

© 2023 The Authors. Advanced Therapeutics published by Wiley-VCH GmbH

23663987, 2024, 2, Downloaded from https://onlinelibrary.wiley.com/doi/10.1002/adtp.202300319 by Koc University, Wiley Online Library on [26/02/2024]. See the Terms and Conditions (https://onlinelibrary.wiley.com/terms-and-conditions) on Wiley Online Library for rules of use; OA articles are governed by the applicable Creative Commons License

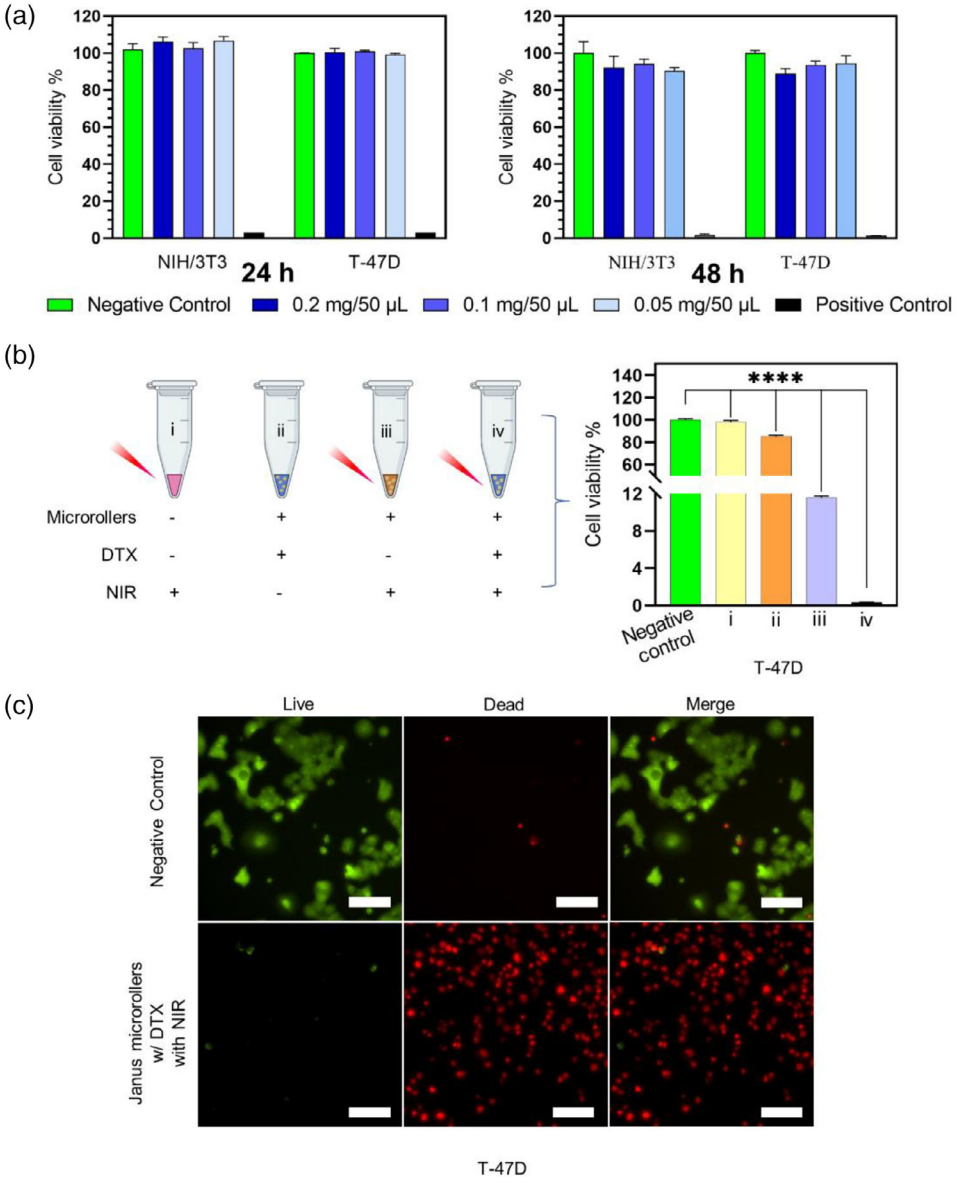


Figure 4. In vitro cell culture studies. A) Biocompatibility test results after 24 and 48 h of the extract test show that no toxic matter was released from DTX free microrollers. B) Cytotoxicity test results after 48 h with and without photothermal ablation. NIR intensity was kept between 2 and 2.7 W cm^{-2} to keep the temperature at 60 °C. T-47D tumor cell death was induced most efficiently by chemo-photothermal ablation combined therapy. (One-way ANOVA, ****$p < 0.05$.) CellTiter-Glo was used for the analysis of ATP levels at (A) and (B); C) Live/Dead microscopy images of T-47D cells, including negative control, and the group underwent photothermal ablation with DTX loaded microrollers were consistent with the analysis of ATP levels after 48 h of incubation. Scale bar: 20 µm. The error bars represent the standard deviation of the mean.

incubation. ATP levels were analyzed at the end of the incubation time. After 48 h, the viability of only NIR applied group (i) was 97%, revealing that NIR itself did not show any cytotoxic effect. The group with DTX containing microrollers (ii) showed 85% of cell viability, indicating that at the given dose, DTX is insufficient to create a severe cytotoxic effect due to its low solubility in the culture media and low permeability from the cell membrane.[57] When the 40 min of photothermal ablation at 60 °C was applied with DTX-free microrollers (iii), the cell viability dramatically decreased to 11%. The most efficient cytotoxic effect (0.4% of cell viability) was achieved when DTX and thermal ablation were combined (iv, Figure 4B). Achieving low viability ratios is critical for reducing the local recurrence rate at the treatment site,[58] and it was only achieved when chemotherapy and photothermal ablation were combined. Similar results were obtained from 24 h of incubation, shown in Figures S7 and S8, Supporting Information. Viability results were further confirmed based on membrane integrity (Live/Dead Cell Imaging) of the NIR applied group with DTX-loaded microrollers (iv) in comparison to a negative control group. As shown in Figure 4C, the treated cells appeared red, indicating death, while the negative control cells were green, indicating life. The images verified the low cell

© 2023 The Authors. Advanced Therapeutics published by Wiley-VCH GmbH

23663987, 2024, 2, Downloaded from https://onlinelibrary.wiley.com/doi/10.1002/adtp.202300319 by Koc University, Wiley Online Library on [26/02/2024]. See the Terms and Conditions (https://onlinelibrary.wiley.com/terms-and-conditions) on Wiley Online Library for rules of use; OA articles are governed by the applicable Creative Commons License

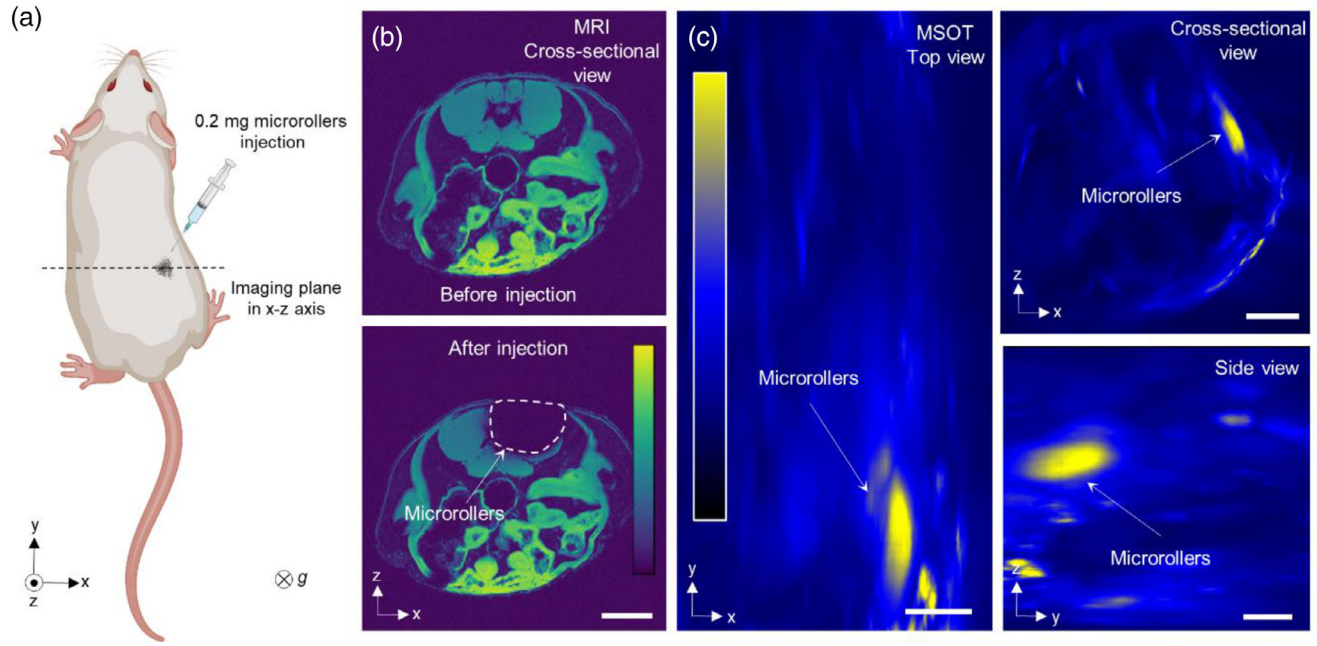


Figure 5. Ex vivo medical imaging of microrollers using magnetic resonance imaging (MRI) and photoacoustic imaging (PA). A) 0.2 mg or 7.8×10^6 microrollers were injected to the back of the dead mouse for imaging experiments. B) Cross-sectional MRI images of the dead-mouse, before and after injection. The magnetic microrollers distorted the MRI image, and the microrollers were easily visible after injection as a big, dark spot. The scale bar is 5 mm. C) PA projection images of the same dead mouse at 900 nm wavelength. The injection was also easily visible in PA imaging from different projections. Scale bar: 5 mm.

viability% caused by DTX and photothermal ablation and were compatible with the data obtained from the analysis of ATP levels.

2.5. Biomedical Imaging Studies

Accurate localization of microrobots within in vivo environments is a crucial prerequisite for realizing the clinical potential of mobile microrobots.[9,11,59–61] The necessary spatial resolution for tracking microrobots in a particular imaging modality depends on the contrast agent used in that modality and its concentration within the microrobot system. In our previous work, we showed that the magnetic thin film coated microrollers can generate more than sufficient contrast in magnetic MRI and PA due to their magnetic and optical contrast, respectively.[11]

To assess the imaging potential of the microrollers used in this study, we injected 0.2 mg microrollers, the dose determined to be effective for photothermal ablation based on in vitro cell culture studies, to the back of a dead mouse and performed MRI and PA imaging (**Figure** 5A). It is important to acknowledge that dynamics between in vitro, ex vivo, and in vivo may vary, and this dose was determined based on the in vitro studies as a starting point. To advance toward in vivo experimentation, a comprehensive and systematic testing approach is required. We anticipated that the presence of a magnetic (Ni) layer on microrollers would lead to signal loss on the gradient echo T2*-weighted images, due to inability of imaging gradients to refocus the signal in the presence of magnetic fields from microrollers. The presence of microrollers thus leads to signal dephasing and hypointense signal regions on T2*-weighted images. As expected, the microrollers created a local negative MRI contrast (dark regions) after the injection and were easy to spot in the axial cross-sectional image (Figure 5B). The microrollers were also readily detectable in PA imaging (Figure 5C) thanks to the magnetic cap allowing the imaging contrast.[11] It is important to note that the spot in the PA image size seemed much smaller than the one in MRI. However, this was expected due to the fact that magnetic materials create region of signal loss multiple times than their actual sizes in MRI.[11,62] Overall, the initial imaging experiments demonstrated that 0.2 mg of microrollers were easily visible in MRI and PA ex vivo.

3. Discussion

In this study, we demonstrated the potential of microrollers for combined synergistic therapy. Specifically, we characterized the photothermal ablation ability, drug release, and magnetic locomotion characteristics of microrollers. The majority of the marketed drugs are poorly water-soluble[20] and are classified as Class II (low solubility, high permeability) and Class IV according to the BCS developed by Amidon et al.[63] DTX is being used to manage and treat solid tumors.[64] Despite its therapeutic potential, the low water solubility and permeability of DTX have limited its applications, and efforts to optimize the formulations are continuing.[64,65] A number of formulation strategies based on increasing the drug dissolution rate or solubility of the drugs have been developed to improve the delivery of BCS Class II and BCS Class IV drugs.[20] Amorphization is one of the most preferred techniques due to its practicality and low cost.[66] Mesoporous

© 2023 The Authors. Advanced Therapeutics published by Wiley-VCH GmbH

23663987, 2024, 2, Downloaded from https://onlinelibrary.wiley.com/doi/10.1002/adtp.202300319 by Koc University, Wiley Online Library on [26/02/2024]. See the Terms and Conditions (https://onlinelibrary.wiley.com/terms-and-conditions) on Wiley Online Library for rules of use; OA articles are governed by the applicable Creative Commons License

silica is a particularly promising material for improving the delivery of poorly water-soluble drugs, as these drugs can be loaded into the nm-sized pores in the amorphous state, resulting in improved dissolution. Therefore, mesoporous silica with a 4 nm pore size was selected in our study and high dissolution rate was achieved thanks to these mesopores. After conducting characterization studies, we confirmed the synergistic therapy potential of microrollers through in vitro cytotoxicity tests.

We also injected the microrollers into the ex vivo tissues of a dead mouse and confirmed the presence of microrollers using MRI and PA techniques. MRI is a long-established imaging modality used in various clinical practices.[62] It operates by exciting nuclear spins with a radio-frequency field and manipulating spin phases using a magnetic field. With its ability to produce high-resolution 3D anatomical images of soft tissues, MRI is a prominent imaging modality for microrobotic tracking.[67,68] PA is also a novel imaging technique that could be utilized for microrobot imaging[11,59,60,69] that relies on detecting ultrasound waves emitted upon the absorption of pulsed laser light from body tissues. The contrast in PA imaging is determined by the optical properties of tissues and microrobots and the wavelength of the applied light. This technique offers great promise in the medical microrobotics field due to its ability to provide micrometer-resolution and real-time imaging.[70] Still, it is important to note that both imaging modalities have advantages and disadvantages. For example, obtaining high-resolution MRI images requires significant time, which disables the imaging-guided navigation of microrollers. Still, MRI is a more conventional and well-established modality and has been shown to be more sensitive than PA for microrollers.[11,62] On the other hand, PA offers high-frequency imaging that is desirable for imaging-guided navigation; however, it also suffers from low penetration ability, and its use is still limited to small-scale animals.[9] Overall, our findings highlight the potential of microrollers for targeted medical interventions in the future, possibly as adjuvant or neoadjuvant therapy.

It must be noted that one of the most important limitations of NIR light is the penetration depth, which is a few millimeters.[71] This limits the clinical applications of superficial tumors or tumors locating inner cavities such as the bladder and colon.[18,71] One of the possible realistic application routes of microrollers includes their deployment to breast ducts via intraductal delivery and magnetic targeting of ductal carcinoma or lobular carcinoma in situ. Toward that goal, extensive in vivo tests must be performed considering real-time medical imaging, biocompatibility aspects, and removal of the microrollers. Another promising deployment route is the circulatory system, at which microrollers have also shown potential.[10,11] The system given here could be used to treat the aneurysms by filling the aneurysm bulge with microrollers,[72] The synergistic mechanism presented here could also be used to induce in the gel like formation in an aneurysm for its superior treatment. Still, all these considerations must be substantiated with further experimental analyses. To overcome the penetration depth issue the potential of alternative heating techniques, such as radio-frequency heating will be explored in future work.

In our study, we sought to expand the medical and pharmaceutical applications of microrollers by focusing on their biological characterizations. While past research concentrated on microroller locomotion and physics,[10–14,73,74] we aimed to broaden their medical and pharmaceutical relevance. Our study stands out for its unique focus on combinational therapy, active magnetic targeting, and enhanced drug dissolution rates integrated into a single microroller platform. We chose DTX, a challenging drug due to its poor solubility and limited permeability, as our primary candidate for active magnetic targeting. Additionally, our microrollers feature coercivity, enabling precise targeting through pre-magnetization, differentiating them from the existing literature.[75–79] Microrollers have a unique advantage in drug delivery due to their active targeting ability, which has the potential to revolutionize conventional chemotherapies by overcoming the problem of non-specific drug distribution. Overall, the design approach presented in this study establishes the realistic medical applications of microrollers, which could lead to their practical use in high-impact medical interventions such as targeted cancer treatment.

4. Experimental Section

Fabrication of Janus Microrollers: 4 mg of silica particles (Sigma-Aldrich, mesoporous, 3 µm particle size, 4 nm pore size) were dispersed in 960 µL of a 1:1 ethanol:ultrapure water mixture. 200 µL of dispersion were spread on a 2.5 cm × 2.5 cm glass substrate by the drop-casting technique and dried inside the fume hood. After bare silica particles were dried, Ni (540 nm) and Au (50 nm) nanofilms were sputtered with predefined tilt angles using a sputter coating system (Leica, EM ACE600), enabling Janus particle formation. The magnetization direction of microrollers was programmed to out-of-plane direction to the surface plane after sputtering by applying a 1.8 T uniform magnetic field to a vibrating sample magnetometer (MicroSense, Lowell, MA). Later, microrollers were released from the substrate using a sonicator bath and dispersed in PBS 1×. SEM images of microrollers were captured via a Zeiss Ultra 550 Gemini scanning electron microscope (Carl Zeiss Inc., Oberkochen, Germany). 118 kV TEM images of bare silica particles were captured via a Hitachi HT7700. 200 kV STEM images of bare silica particles were captured via a Hitachi HF5000 200 kV (S)TEM. Absorbance values were recorded from 400 to 1000 nm wavelengths with ultraviolet (UV)/visible/NIR spectroscopy (PerkinElmer, Lambda 1050).

Photothermal Heating Setup: Photothermal heating setup is shown in Figure S2, Supporting Information. 808 nm NIR light was used for heating the microrollers (B&W Tek Inc., BWF1 808 nm, 450 mW). The tip of the NIR light with a collimator (THORLABS, F240SMA-780) was fixed 12.5 cm above the microrollers. A thermal infrared camera (FLIR, ETS320) positioned 8.5 cm above the microrollers to monitor the temperature change continuously. Microrollers were dispersed in 50 µL PBS in concentrations of 0.2 mg/50 µL, 0.1 mg/50 µL, and 0.05 mg/50 µL. Microrollers were immobilized at the bottom of a centrifuge tube using a permanent magnet, allowing for precise irradiation of NIR light onto the microrollers. To avoid the NIR light from focusing on the magnet itself, it was kept 1 cm away from the tube and the microrollers.

Phantom Preparation: A tissue mimicking agar phantom was prepared with Intralipid 20% emulsion (Sigma-Aldrich) and black ink (Pelikan) for scattering and absorbing properties, respectively. 0.45 g of agar (VWR Chemicals) was dissolved in 30 mL ultrapure water. intralipid 20% emulsion (0.62 mL) was heated in a hot water bath, added to the hot agar solution, and mixed gently. The ink (0.6 mL of 1:100 diluted stock in ultrapure water) was added to the agar and intralipid mixture, followed by a gentle mix. 3.9 mL of the prepared solution was poured into a petri dish and cooled at room temperature. After 30 min, it solidified and formed a 0.5 mm thick phantom.

Determination of DTX Amount via HPLC Studies: An Agilent 1260 Infinity II HPLC system and OpenLab CDS software were used for instrument operation control and data collection. Agilent Poroshell 120 EC C18

© 2023 The Authors. Advanced Therapeutics published by Wiley-VCH GmbH

23663987, 2024, 2, Downloaded from https://onlinelibrary.wiley.com/doi/10.1002/adtp.202300319 by Koc University, Wiley Online Library on [26/02/2024]. See the Terms and Conditions (https://onlinelibrary.wiley.com/terms-and-conditions) on Wiley Online Library for rules of use; OA articles are governed by the applicable Creative Commons License

(2.7 µm, 3 × 100 mm) column was employed for separation using isocratic elution with a flow rate of 0.8 mL min^{-1}, 10 µL injection volume, and a mobile phase consisting of acetonitrile (ACN) and water 48:52. The system was conditioned at room temperature, and the analysis time was 5 min. The retention time was 2.8 min at 230 nm. The described method was validated according to the ICH Q2 (R1) guideline for accuracy, precision (repeatability, intermediate precision), specificity, linearity, and robustness.[80]

Nile Red and DTX Loading Studies: Nile red (Sigma-Aldrich) solutions in the concentration of 0.3 mg mL^{-1} were prepared in ethanol, DCM, and 2:1 DCM:hexane (Figure S3A, Supporting Information). 10 mg of bare silica particles were added to the 1 mL of mixtures separately and vortexed for 6 h at 1000 rpm at room temperature. At the end of 6 h, Nile red loaded silica particles were washed with their respective solvents three times using centrifugation and dried under vacuum overnight (Figure S3B, Supporting Information). Nile red loaded silica particles were dispersed in PBS after complete drying.

In order to compare the EE% of DTX (Sigma-Aldrich) loaded with DCM versus 2:1 DCM:hexane, 2 mg of DTX was dissolved in either 1 mL of DCM or 2:1 DCM:hexane mixture. 6 mg of microrollers were added to the mixture and then subjected to the loading procedure described above. After the loading and drying steps were completed, loaded DTX was extracted from the silica particles via ACN by vigorous vortexing followed by sonication. Extracts were injected to the HPLC, and EE% was calculated according to Equation (1). For all subsequent experiments, the same DTX loading steps were followed, as well as the ratio of 1:3 for DTX to bare silica or microrollers.

$$EE\% = \frac{\text{Amount of drug loaded into particles}}{\text{Initial drug amount}} \times 100 \quad (1)$$

ATR FT-IR spectra were recorded from 3500 to 400 cm^{-1} with Bruker, Tensor II. TGA was performed between 25–350 °C with Perkin Elmer, TGA 4000. BET analysis was performed with Anton Paar, Nova 600. DSC analysis was performed between 25–200 °C with TA Instruments, DSC 2500. 2theta-omega XRD scans were recorded with Bruker, D8 Discover.

Drug Release Studies: Drug release studies were carried out in a 0.1% Tween 80 (Sigma-Aldrich) containing PBS solution. Tween 80 was used to improve the solubility of DTX.[81] The pH of the release media was adjusted to 6.8 to simulate the tumor environment.[82] DTX loaded microrollers were dispersed in 1 mL release media in the centrifuge tubes and placed into a thermoshaker at 37 °C and 750 rpm. 500 µL of samples were withdrawn at pre-determined time intervals and replaced with fresh release media to maintain the sink condition. The DTX amount in these samples was evaluated cumulatively by the validated HPLC method, as previously described. DDSolver program was used to analyze the kinetics of the dissolution profile of DTX.

Extract Test: NIH/3T3 (ATCC) cells were cultured in Dulbecco's Modified Eagle's Medium (DMEM, Gibco), supplemented with 10% fetal bovine serum (FBS, Gibco) and 1% penicillin/streptomycin (Gibco) in a humidified 37 °C and 5% CO_2 atmosphere using a black/clear bottom 96-well plate (Corning). 1×10^4 cells per well were seeded the day before the experiment. T-47D cells were cultured in RPMI-1640 medium (Gibco), supplemented with 10% FBS (Gibco) and 1% penicillin/streptomycin (Gibco) in a humidified 37 °C and 5% CO_2 atmosphere. Similar to NIH/3T3 cells, T-47D (ATCC) cells were seeded in a black/clear bottom 96-well plate at a concentration of 1×10^4 cells per well the day before the experiment. Microrollers were dispersed in PBS 1× and kept at 70 ± 2 °C for 24 and 48 h by agitating with an orbital shaker. Before applying to cells, the supernatants were diluted with cell culture mediums to obtain three concentrations as follows: 0.2 mg/50 µL, 0.1 mg/50 µL, and 0.05 mg/50 µL. After 24 h of incubation, the viability of the cells was analyzed depending on the ATP levels using the CellTiter-Glo assay (Promega). The luminescence of the cell lysates was measured with a microplate reader (BioTek Synergy 2). 20% Triton X-100 (Sigma-Aldrich) in cell culture medium was used as the positive control, and the cells treated only with cell culture medium were used as the negative control.

Photothermal Ablation: A total of 5×10^5 T-47D (ATCC) cells were centrifuged at 1500 rpm for 4 min, together with i) no microrollers, with NIR, ii) microrollers w/DTX, no NIR, iii) DTX free microrollers, with NIR, and iv) microrollers w/DTX, with NIR in 50 µL of RPMI-1640 (Gibco) medium supplemented with FBS (Gibco) and penicillin/streptomycin (Gibco). Microroller quantity was 0.2 mg for (ii), (iii), and (iv). NIR light was applied for 40 min to (i), (iii), and (iv) while (ii) was kept in the incubator. At the end of 40 min, the pellet was dispersed, and cells were diluted to have a concentration of 1×10^4 cells/100 µL. A black/clear bottom 96-well plate (Corning) was seeded at a concentration of 1×10^4 cells per well while the microrollers kept inside the stock solution via a permanent magnet. After 24 and 48 h of incubation, the amount of ATP in the cells was measured using CellTiter-Glo assay (Promega), according to the supplier's instructions. To provide visual evidence, a parallel set of T-47D cells were seeded to microwells (µ-Slide, 8 Well, ibidi) at a concentration of 15×10^3 cells per well and stained in Live/Dead Cell Imaging Kit (Invitrogen) as specified by the vendor. Images of live (calcein-AM) (Ex/Em: 488/520 nm) and dead (ethidium homodimer-1) (Ex/Em: 528/617 nm) cells were obtained using a fluorescent microscope (Nikon Eclipse Ti-E) after 24 and 48 h of incubation.

MRI and PA Imaging: MRI was performed on 7 T Bruker BioSpec (Ettlingen, Germany) using an actively shielded gradient system (BGA20SHP) and a 40 mm quadrature birdcage coil. Gradient echo imaging sequence (TR = 500 ms, TE = 7 ms, 100 × 100 µm 2 in plane resolution, 0.5 mm slice thickness, NEX = 2) was used to image mice before and after injection of 0.2 mg of microrollers. The whole-body scan was performed in a multispectral optoacoustic tomography device (MSOT 512-element transducer, iThera Medical) system with a scanning step of 0.3 mm at 900 nm wavelengths.

Statistical Analysis: All quantitative values are presented as means ± SD of the mean.

Supporting Information

Supporting Information is available from the Wiley Online Library or from the author.

Acknowledgements

This work was funded by the Max Planck Society and the Scientific and Technological Research Council of Turkey-TUBITAK (2214-A International Research Fellowship Programme for Ph.D. Students). The authors thank A. Shiva for SEM imaging and VSM analysis, E. Azizoglu, G. Arslan Azizoglu, and N. Z. Arda Ozturk for HPLC discussions, S. Feyzi and S. Giray for BET analysis and discussions, G. Y. Turkyilmaz and M. A. Ege for kinetics of the drug dissolution profiles discussions, and A. Motallebzadeh for further BET analysis. The cartoons in Figures 2A and 4B were created with Biorender.com. Open access funding was enabled and organized by Project DEAL. The authors thank Max Planck Institute for Biological Cybernetics Tübingen (reg: DE 08 416 1083 21) for providing animal side products to MPI Intelligent Systems in Stuttgart (reg: DE 08 111 1008 21) to perform the ex vivo dead mice experiments.

Open access funding enabled and organized by Projekt DEAL.

Conflict of Interest

The authors declare no conflict of interest.

Data Availability Statement

The data that support the findings of this study are available from the corresponding author upon reasonable request.

© 2023 The Authors. Advanced Therapeutics published by Wiley-VCH GmbH

23663987, 2024, 2, Downloaded from https://onlinelibrary.wiley.com/doi/10.1002/adtp.202300319 by Koc University, Wiley Online Library on [26/02/2024]. See the Terms and Conditions (https://onlinelibrary.wiley.com/terms-and-conditions) on Wiley Online Library for rules of use; OA articles are governed by the applicable Creative Commons License

Keywords

chemotherapy, combination therapy, Janus microrollers, medical microrobotics, photothermal ablation

Received: October 30, 2023
Published online: November 27, 2023

[1] K. Park, *ACS Nano* **2013**, *7*, 7442.
[2] M. Sitti, *Mobile Microrobotics*, The MIT Press, Cambridge, MA **2017**.
[3] B. J. Nelson, I. K. Kaliakatsos, J. J. Abbott, *Annu. Rev. Biomed. Eng.* **2010**, *12*, 55.
[4] G. Tezel, S. S. Timur, F. Kuralay, R. N. Gürsoy, K. Ulubayram, L. Öner, H. Eroglu, *J. Drug Targeting* **2021**, *29*, 29.
[5] J. Jiang, Z. Yang, A. Ferreira, L. I. Zhang, *Adv. Intell. Syst.* **2022**, *4*, 2100279.
[6] D. Liu, T. Wang, Y. Lu, *Adv. Healthcare Mater.* **2022**, *11*, 2102253.
[7] S. Wang, X. Liu, Y. Wang, D. Xu, C. Liang, J. Guo, X. Ma, *Nanoscale* **2019**, *11*, 14099.
[8] N. O. Dogan, H. Ceylan, E. Suadiye, D. Sheehan, A. Aydin, I. C. Yasa, A.-M. Wild, G. Richter, M. Sitti, *Small* **2022**, *18*, 2204016.
[9] A. Aziz, S. Pane, V. Iacovacci, N. Koukourakis, J. Czarske, A. Menciassi, M. Medina-Sánchez, O. G. Schmidt, *ACS Nano* **2020**, *14*, 10865.
[10] Y. Alapan, U. Bozuyuk, P. Erkoc, A. C. Karacakol, M. Sitti, *Sci. Rob.* **2020**, *5*, eaba5726.
[11] U. Bozuyuk, E. Suadiye, A. Aghakhani, N. O. Dogan, J. Lazovic, M. E. Tiryaki, M. Schneider, A. C. Karacakol, S. O. Demir, G. Richter, M. Sitti, *Adv. Funct. Mater.* **2022**, *32*, 2109741.
[12] U. Bozuyuk, Y. Alapan, A. Aghakhani, M. Yunusa, M. Sitti, *Proc. Natl. Acad. Sci. USA* **2021**, *118*, e2022090118.
[13] U. Bozuyuk, A. Aghakhani, Y. Alapan, M. Yunusa, P. Wrede, M. Sitti, *Nat. Commun.* **2022**, *13*, 6289.
[14] U. Bozuyuk, H. Ozturk, M. Sitti, *Adv. Intell. Syst.* **2023**, *5*, 2300099.
[15] X. Qi, S. Wang, S. Ma, K. Han, X. Bian, X. Li, *Phys. Fluids* **2021**, *33*, 121908.
[16] Z. Wu, Y. Zhang, N. Ai, H. Chen, W. Ge, Q. Xu, *Adv. Intell. Syst.* **2022**, *4*, 2100266.
[17] W. Fan, B. Yung, P. Huang, X. Chen, *Chem. Rev.* **2017**, *117*, 13566.
[18] J. Beik, Z. Abed, F. S. Ghoreishi, S. Hosseini-Nami, S. Mehrzadi, A. Shakeri-Zadeh, S. K. Kamrava, *J. Controlled Release* **2016**, *235*, 205.
[19] Q. Dai, B. Cao, S. Zhao, A. Zhang, *Bioengineering* **2022**, *9*, 474.
[20] R. Ghadi, N. Dand, *J. Controlled Release* **2017**, *248*, 71.
[21] X. Cui, Q. Ruan, X. Zhuo, X. Xia, J. Hu, R. Fu, Y. Li, J. Wang, H. Xu, *Chem. Rev.* **2023**, *123*, 6891.
[22] S. Okuyama, T. Nagaya, F. Ogata, Y. Maruoka, K. Sato, Y. Nakamura, P. L. Choyke, H. Kobayashi, *OncoTargets Ther.* **2017**, *8*, 113194.
[23] S. N. Goldberg, G. S. Gazelle, P. R. Mueller, *Am. J. Roentgenol.* **2000**, *174*, 323.
[24] M. Nikfarjam, V. Muralidharan, C. Christophi, *J. Surg. Res.* **2005**, *127*, 208.
[25] M. B. Akolpoglu, Y. Alapan, N. O. Dogan, S. F. Baltaci, O. Yasa, G. Aybar Tural, M. Sitti, *Sci. Adv.* **2022**, *8*, 6163.
[26] R. Mellaerts, J. A. G. Jammaer, M. Van Speybroeck, C. Hong, J. Van Humbeeck, P. Augustijns, G. Van Den Mooter, J. A. Martens, *Langmuir* **2008**, *24*, 8651.
[27] K. Trzeciak, A. Chotera-Ouda, I. I. Bak-Sypien, M. J. Potrzebowski, *Pharmaceutics* **2021**, *13*, 950.
[28] K. B. Seljak, P. Kocbek, M. Gasperlin, *J. Drug Delivery Sci. Technol.* **2020**, *59*, 101906.
[29] C. Charnay, S. Bégu, C. Tourné-Péteilh, L. Nicole, D. A. Lerner, J. M. Devoisselle, *Eur. J. Pharm. Biopharm.* **2004**, *57*, 533.
[30] ICH Harmonised Guideline Impurities: Guideline for Residual Solvents Q3C(R8), International Council For Harmonisation Of Technical Requirements for Pharmaceuticals for Human Use, Geneva, Switzerland **2021**.
[31] C. Reichardt, T. Welton, *Solvents and Solvent Effects in Organic Chemistry*, Wiley-VCH Verlag GmbH & Co. KGaA, Hoboken, NJ **2010**.
[32] P. G. Jessop, D. A. Jessop, D. Fu, L. Phan, *Green Chem.* **2012**, *14*, 1245.
[33] R. Plenderleith, T. Swift, S. Rimmer, *RSC Adv.* **2014**, *4*, 50932.
[34] K. Trzeciak, S. Kazmierski, E. Wielgus, M. J. Potrzebowski, *Microporous Mesoporous Mater.* **2020**, *308*, 110506.
[35] V.-P. Lehto, K. Vähä-Heikkilä, J. Paski, J. Salonen, *J. Therm. Anal. Calorim.* **2005**, *80*, 393.
[36] A. Hillerström, M. Andersson, J. Samuelsson, J. Van Stam, *Colloid Interface Sci. Commun.* **2014**, *3*, 5.
[37] H. Wu, Y. U. Xiao, Y. U. Guo, S. Miao, Q. Chen, Z. Chen, *Microporous Mesoporous Mater.* **2020**, *292*, 109754.
[38] N. I. Hammadi, Y. Abba, M. N. M. Hezmee, I. S. A. Razak, A. Z. Jaji, T. Isa, S. K. Mahmood, M. Z. A. B. Zakaria, *Pharm. Res.* **2017**, *34*, 1193.
[39] M. C. O. Da Rocha, P. B. Da Silva, M. A. Radicchi, B. Y. G. Andrade, J. V. De Oliveira, T. Venus, C. Merker, I. Estrela-Lopis, J. P. F. Longo, S. N. Báo, *J Nanobiotechnology* **2020**, *18*, 43.
[40] W. Xu, J. Riikonen, V.-P. Lehto, *Int. J. Pharm.* **2013**, *453*, 181.
[41] T. Heikkilä, J. Salonen, J. Tuura, N. Kumar, T. Salmi, D. Y. U. Murzin, M. S. Hamdy, G. Mul, L. Laitinen, A. M. Kaukonen, J. Hirvonen, V.-P. Lehto, *Drug Delivery* **2007**, *14*, 337.
[42] L. K. Tatini, K. V. S. R. Krishna Reddy, N. Someswara Rao, *AAPS PharmSciTech* **2012**, *13*, 548.
[43] D. N. Bikiaris, *Expert Opin. Drug Delivery* **2011**, *8*, 1663.
[44] P. Kinnari, E. Mäkilä, T. Heikkilä, J. Salonen, J. Hirvonen, H. A. Santos, *Int. J. Pharm.* **2011**, *414*, 148.
[45] Y. Zhang, Z. Zhi, T. Jiang, J. Zhang, Z. Wang, S. Wang, *J. Controlled Release* **2010**, *145*, 257.
[46] J. Salonen, L. Laitinen, A. M. Kaukonen, J. Tuura, M. Björkqvist, T. Heikkilä, K. Vähä-Heikkilä, J. Hirvonen, V.-P. Lehto, *J. Controlled Release* **2005**, *108*, 362.
[47] C. G. Keum, Y. W. Noh, J. S. Baek, J. H. Lim, C. J. Hwang, Y. G. Na, S. C. Shin, C. W. Cho, *Int. J. Nanomed.* **2011**, *6*, 2225.
[48] M. P. Paarakh, P. A. N. I. Jose, C. M. Setty, G. V. Peter, *Int. J. Pharm. Res. Technol.* **2018**, *8*, 12.
[49] R. M. Sábio, A. B. Meneguin, T. C. Ribeiro, R. R. Silva, M. Chorilli, *Int. J. Pharm.* **2019**, *564*, 379.
[50] C. A. Aerts, E. Verraedt, R. Mellaerts, A. Depla, P. Augustijns, J. Van Humbeeck, G. Van Den Mooter, J. A. Martens, *J. Phys. Chem. C* **2007**, *111*, 13404.
[51] T. O. Tasci, P. S. Herson, K. B. Neeves, D. W. M. Marr, *Nat. Commun.* **2016**, *7*, 10225.
[52] USP Biological Reactivity Tests, In Vitro, United States Pharmacopeial Convention, North Bethesda, MD **2015**.
[53] ISO 10993–5 Biological Evaluation of Medical Devices Part:5: Tests for In Vitro Cytotoxicity, ISO, Geneva, Switzerland **2009**.
[54] N. O. Dogan, U. Bozuyuk, P. Erkoc, A. C. Karacakol, A. Cingoz, F. Seker-Polat, M. A. Nazeer, M. Sitti, T. Bagci-Onder, S. Kizilel, *Adv. Nanobiomed. Res.* **2022**, *2*, 2100033.
[55] Guidance Document on Using In Vitro Data to Estimate In Vivo Starting Doses for Acute Toxicity, NIH Publication, Bethesda, MD **2001**.
[56] T. Tsuchiya, *J. Biomater. Appl.* **1994**, *9*, 138.
[57] M. F. Sohail, M. Rehman, H. S. Sarwar, S. Naveed, O. S. Qureshi, N. I. Bukhari, I. Hussain, T. J. Webster, G. Shahnaz, *Int. J. Nanomed.* **2018**, *13*, 3145.
[58] M. Ahmed, M. Moussa, S. N. Goldberg, *Chem. Phys. Lipids* **2012**, *165*, 424.
[59] P. Wrede, O. Degtyaruk, S. K. Kalva, X. L. Deán-Ben, U. Bozuyuk, A. Aghakhani, B. Akolpoglu, M. Sitti, D. Razansky, *Sci. Adv.* **2022**, *8*, 9132.

© 2023 The Authors. Advanced Therapeutics published by Wiley-VCH GmbH

23663987, 2024, 2, Downloaded from https://onlinelibrary.wiley.com/doi/10.1002/adtp.202300319 by Koc University, Wiley Online Library on [26/02/2024]. See the Terms and Conditions (https://onlinelibrary.wiley.com/terms-and-conditions) on Wiley Online Library for rules of use; OA articles are governed by the applicable Creative Commons License

[60] A. Aziz, J. Holthof, S. Meyer, O. G. Schmidt, M. Medina-Sánchez, *Adv. Healthcare Mater.* **2021**, *10*, 2101077.
[61] Q. Wang, K. F. Chan, K. Schweizer, X. Du, D. Jin, S. C. H. O. Yu, B. J. Nelson, L. I. Zhang, *Sci. Adv.* **2021**, *7*, 5914.
[62] O. Erin, M. Boyvat, M. E. Tiryaki, M. Phelan, M. Sitti, *Adv. Intell. Syst.* **2020**, *2*, 1900110.
[63] G. L. Amidon, H. Lennernäs, V. P. Shah, J. R. Crison, *Pharm. Res.* **1995**, *12*, 413.
[64] F. Andisheh, F. Oroojalian, N. Shakour, M. Ramezani, J. Shamsara, E. Khodaverdi, H. Nassirli, F. Hadizadeh, M. Alibolandi, *Int. J. Pharm.* **2021**, *605*, 120822.
[65] H. Kim, Y. Lee, I. N.-H. Lee, S. Kim, D. Kim, P. E. R. Saw, J. Lee, M. Choi, Y.-C. Kim, S. Jon, *J. Controlled Release* **2014**, *178*, 118.
[66] T.-T. U. Le, A. K. Elzhry Elyafi, A. R. Mohammed, A. Al-Khattawi, *Pharmaceutics* **2019**, *11*, 269.
[67] M. E. Tiryaki, S. O. Demir, M. Sitti, *IEEE Rob. Autom. Lett.* **2022**, *7*, 6982.
[68] M. E. Tiryaki, M. Sitti, *Adv. Intell. Syst.* **2022**, *4*, 2100178.
[69] Z. Wu, L. Li, Y. Yang, P. Hu, Y. Li, S. Y. Yang, L. V. Wang, W. Gao, *Sci. Rob.* **2019**, *4*, eaax0613.
[70] S. Gottschalk, O. Degtyaruk, B. Mc Larney, J. Rebling, M. A. Hutter, X. L. Deán-Ben, S. Shoham, D. Razansky, *Nat. Biomed. Eng.* **2019**, *3*, 392.
[71] Y. Alapan, O. Yasa, O. Schauer, J. Giltinan, A. F. Tabak, V. Sourjik, M. Sitti, *Sci. Rob.* **2018**, *3*, eaar4423.
[72] A. C. Bakenecker, A. Von Gladiss, H. Schwenke, A. Behrends, T. Friedrich, K. Lüdtke-Buzug, A. Neumann, J. Barkhausen, F. Wegner, T. M. Buzug, *Sci. Rep.* **2021**, *11*, 14082.
[73] U. Bozuyuk, E. Yildiz, M. Han, S. O. Demir, M. Sitti, *Small* **2023**, 2303396, doi: https://doi.org/10.1002/smll.202303396.
[74] U. Bozuyuk, H. Ozturk, M. Sitti, *Sci. Rep.* **2023**, *13*, 10196.
[75] J. Han, J. Zhen, V. Du Nguyen, G. Go, Y. Choi, S. Y. Ko, J.-O. H. Park, S. Park, *Sci. Rep.* **2016**, *6*, 28717.
[76] L. I.-S. Lin, X. Yang, Z. Zhou, Z. Yang, O. Jacobson, Y. Liu, A. Yang, G. Niu, J. Song, H.-H. Yang, X. Chen, *Adv. Mater.* **2017**, *29*, 1606681.
[77] D. E. Gong, N. Celi, D. Zhang, J. Cai, *ACS Appl. Mater. Interfaces* **2022**, *14*, 6320.
[78] D. Jin, K. E. Yuan, X. Du, Q. Wang, S. Wang, L. I. Zhang, *Adv. Mater.* **2021**, *33*, 2100070.
[79] X. Song, Z. Chen, X. Zhang, J. Xiong, T. Jiang, Z. Wang, X. Geng, U. K. Cheang, *Sci. Rep.* **2021**, *11*, 7907.
[80] ICH Harmonised Tripartite Guideline Validation of Analytical Procedures: Text and Methodology Q2(R1), International Conference On Harmonisation Of Technical Requirements For Registration Of Pharmaceuticals For Human Use, Geneva, Switzerland **2005**.
[81] Y. U. Mi, X. Liu, J. Zhao, J. Ding, S. I.-S. Feng, *Biomaterials* **2012**, *33*, 7519.
[82] M. Stubbs, P. M. J. Mcsheehy, J. R. Griffiths, C. L. Bashford, *Mol. Med. Today* **2000**, *6*, 15.

© 2023 The Authors. Advanced Therapeutics published by Wiley-VCH GmbH

23663987, 2024, 2, Downloaded from https://onlinelibrary.wiley.com/doi/10.1002/adtp.202300319 by Koc University, Wiley Online Library on [26/02/2024]. See the Terms and Conditions (https://onlinelibrary.wiley.com/terms-and-conditions) on Wiley Online Library for rules of use; OA articles are governed by the applicable Creative Commons License